RSC Advances

PAPER

View Article Online
View Journal | View Issue

Cite this: *RSC Adv.*, 2017, **7**, 30707

Prediction of magnetoresistance using a magnetic field and correlation between the magnetic and electrical properties of $La_{0.7}Bi_{0.05}Sr_{0.15}Ca_{0.1}Mn_{1-x}In_xO_3$ ($0 \leq x \leq 0.3$) manganite†

Arwa Belkahla,[a] K. Cherif,[a] J. Dhahri,*[a] K. Taibi[b] and E. K. Hlil[c]

In this paper, we have systematically investigated the effect of In doping on the magnetic and magnetocaloric effect (MCE) in $La_{0.7}Bi_{0.05}Sr_{0.15}Ca_{0.1}Mn_{1-x}In_xO_3$ ($0 \leq x \leq 0.3$) manganite. All of the samples exhibit a second-order magnetic phase transition from the ferromagnetic to the paramagnetic state at the Curie temperature (T_C). From the measurements of isothermal magnetization around (T_C), we have determined the magnetic entropy change (ΔS_M). It has been found that there was a large (ΔS_M), *i.e.* a large (MCE), in all samples. Among them, a maximum (ΔS_M) and the highest relative cooling power (RCP) under the magnetic field of 5 T are found to be 6.14 J kg^{-1} K^{-1} and 281 J kg^{-1}, respectively for $x = 0$. This investigation suggests that our samples would be suitable candidates for magnetic refrigeration technology. The relationship between resistivity and magnetization was performed as $\rho = \rho_0 \exp(-M/\alpha)$. The (MCE) was investigated based on the resistivity measurements. The obtained results were discussed. A typical numerical method (Gauss function) was used for fitting the experimental data of resistivity. The simulation values such as metal–semiconductor transition temperature (T_{M-Sc}) and maximum resistivity (ρ_{max}), calculated from this function, showed promising agreement with the experimental data. The shifts of these values as a function of magnetic field for all samples have been interpreted.

Received 14th April 2017
Accepted 6th June 2017

DOI: 10.1039/c7ra04256f

rsc.li/rsc-advances

1. Introduction

Since the discovery of the magnetocaloric effect (MCE) and colossal magnetoresistance (CMR) in perovskite-type oxide materials, the correlation between structure, magnetic, electrical, and transport properties has become a hotspot in today's research.[1–6]

The MCE is the tendency of certain materials, to heat up or cool down during the application or removal of an external magnetic field. This phenomenon is an intrinsic property of magnetic materials and occurs due to the change in the alignment of the magnetic moments under an applied magnetic field. Commonly, the MCE is considered as the entropy change of the system in an isothermal process on applying field. Traditionally, the double-exchange (DE) model[7] was suggested to understand the CMR behavior observed in these materials. In this model, a ferromagnetic (FM) interaction between the localized t_{2g} spins resulted from the hopping of itinerant e_g spins between adjacent Mn atoms subject to strong intra-site Hund's rule coupling. However, it has been found that the (DE) and the super-exchange (SE) mechanism are known to be sensitive to variation in the Mn–O–Mn bond angle and Mn–O bond length, both controlled by the average size of the A- or the B-site ions whereas the density of charge carriers is controlled by the Mn^{3+}/Mn^{4+} ratio.[8–10]

Most of these materials with general formula $R_{1-x}A_xMnO_3$ (where R is the rare-earth element, A is the divalent metal element and x is the doping level) have recently attracted considerable research interest in view of their fascinating fundamental properties such as magneto-resistance, magneto-caloric, charge ordering, phase separation, spin ordering, *etc.*, leading to potential application in magnetic, magneto-electronic, photonic devices, infrared detector, as well as spin-tronics technology.[11]

Experimentally, manganese oxides, especially, the La–Sr based manganite ($La_{0.7}Sr_{0.3}MnO_3$) are very familiar system. It exhibits a metal–semiconductor transition accompanied by a ferromagnetic–paramagnetic transition near the Curie temperature T_C. There are several reports on the magnetocaloric

[a]Laboratoire de la Matière Condensée et des Nanosciences, Département de Physique, Faculté des Sciences de Monastir, 5019, Tunisia. E-mail: jemai_3000@yahoo.com
[b]Laboratoire de Science et Génie des Matériaux, Faculté de Génie Mécanique et Génie des Procédés, Université des Sciences et de la Technologie Houari Boumediene BP32 El Alia, Bab Ezzouar, 16111, Algiers, Algeria
[c]Institut Neel, CNRS et Université Joseph Fourier, B, P, 166, 38042 Grenoble, France

† Electronic supplementary information (ESI) available. See DOI: 10.1039/c7ra04256f

properties of that compound where the large magnetic entropy change with a narrow range of working temperatures was reported at the vicinity of the transition temperature.[12–14] The range of working temperature, as well as the transition temperature were modified by suitable substitutions of Sr and/or Mn ions by other ions.[15,16] In addition, low-level substitution of Mn by Ni (2%) in $La_{0.7}Sr_{0.3}MnO_3$ was found to enhance the magnetic entropy change (6.52 J kg^{-1} K^{-1} at an applied field of 5 T) and shift the transition temperature to above room temperature (350 K).[17]

More recently, a close interplay between magnetic structure and transport properties of these compounds has been explained by means of the (SE) and (DE) interactions, which are accompanied by the strong Jahn–Teller (JT) distortion and electron–phonon interaction arising from the deformation of the $Mn^{3+}O_6$ octahedral.[18] According to (JT) distortion, the structure will distort by removing the degeneracy of the e_g orbitals, to stabilize in the $3d_{3Z^2-r^2}$ with respect to the $3d_{x^2-y^2}$ orbitals.[19] In this context, Xiong *et al.* also found a strong correlation between resistivity and magnetic-entropy change (ΔS_M).[20] So, we can calculate ΔS_M based on the electrical measurement.

In a recent publication,[21–23] there have been few models that can explain the conductive mechanism in our materials. Among those models, we point out the Mott's variable range hopping (VRH) and small polaron hopping (SPH) model in the semiconducting region and electron–electron, electron–phonon processes in the metallic region. To the best of our knowledge, no studies have been done on the mathematical model which can describe the carrier transport behavior of manganite as a function of temperature around the electrical phase transition and the relation between electrical and magnetic properties is a subject which is not much treated.

In this contribution, the first objective of this work is to determine the correlation between electrical and magnetic properties. The second objective is to develop a mathematical model to quantitatively analyze the temperature-dependent resistivity.

2. Experimental details

$La_{0.7}Bi_{0.05}Sr_{0.15}Ca_{0.1}Mn_{1-x}In_xO_3$ ($0 \le x \le 0.3$) compounds were synthesized by Pechini sol–gel method[24] using stoichiometric amounts of $La(NO_3)_3$–$6H_2O$, $Bi(NO_3)_3$–$5H_2O$, $In(NO_3)_3 \cdot xH_2O$, $Sr(NO_3)_2$, $Ca(NO_3)_2$, $Mn(NO_3)_2$–$4H_2O$ (having a purity of more than 99.9% for each of them). Firstly, the reagents were dissolved in distilled water to obtain a mixed solution. Subsequently, when the nitrates were completely dissolved in the solution, citric acid (CA) and ethylene glycol (EG) were added in the required stoichiometric ratio. The process was heated first at 340–380 K with a vigorous stirring to evaporate water, increase viscosity and accelerate the poly-esterification reaction between CA and EG. Then the temperature was raised up to 450 K forming a dark viscous gel which slowly turned into a dark resin at 500 K. This resin was easily powdered in an agate mortar and was calcined at 870 K for 6 h in oxygen atmosphere to eliminate the carbons gases and the other organic compounds. Finally, at 1075 K for 10 h in following air synthesis the resulting powders were uniaxial pressed at 10^5 Pa into circular pellets with a thickness of 2 mm and diameter of 8 mm. The obtained black pellets were then sintered in an oxygen atmosphere at 1273 K for 48 h.

The structure, the crystallinity and phase purity of the sample were checked by powder X-ray diffraction (XRD) measurements made at room temperature using "PANalytical X'Pert Pro" diffractometer with CuKα radiation ($\lambda = 1.5406$ Å). Data acquisition was done in the range of 2θ from 10 to 100° with a step size of 0.017° and a counting time of 18 s per step.

Structural analysis was carried out by the standard Rietveld method[25] using the FULLPROF program.[26]

Magnetization *vs.* temperature (5–450 K) was measured in an applied magnetic field of 0.05 T, using BS1 and BS2 magnetometers developed in Louis Neel Laboratory of Grenoble. The resistivity of these samples was carried out by using the standard four probe method in the temperature range 5–600 K.

3. Results and discussion

3.1. XRD analysis

Fig. 1 shows the X-ray diffraction patterns for the $La_{0.7}Bi_{0.05}Sr_{0.15}Ca_{0.1}Mn_{1-x}In_xO_3$ ($x = 0.1$, 0.2) compounds. No impurity peaks are observed in the pattern, indicating a single-phase formation of all samples. For all the samples, all peaks are satisfactorily indexed in the rhombohedra structure with space group $R\bar{3}c$, hexagonal setting ($Z = 6$), in which the La/Bi/Sr/Ca atoms are at 6a (0, 0, $\frac{1}{4}$), Mn/In at 6b (0, 0, 0) and O at 18e (x, 0, $\frac{1}{4}$) positions. This profile has reasonable *R*-factors and excellent fits between calculated and observed patterns. We have listed the lattice parameters, unit cell volume, and fitting parameters in Table 1. It is seen that the lattice parameters and unit cell volume gradually increase with increasing In concentration. This can be attributed to the average ionic radius of the B-site $\langle r_B \rangle$ which increases systematically as smaller Mn^{3+} ions (0.645) are replaced by larger In^{3+} ions (0.8).[27]

The stability of perovskite sample is usually described in terms of Goldschmidt's tolerance factor (t), which can be calculated using the expression[28]

$$t = \frac{\langle r_{La/Bi/Sr/Ca} \rangle + \langle r_O \rangle}{\sqrt{2}\left(\langle r_{Mn/In} \rangle + \langle r_O \rangle\right)} \quad (1)$$

where $\langle r_{La/Bi/Sr/Ca} \rangle$, $\langle r_{Mn/In} \rangle$ and $\langle r_O \rangle$ are the average ionic radii of the A-site, B-site and O ions, respectively.

Most materials that are stable in the perovskite structure have (t) between 0.75 and 1.05. For all samples, (t) is well below 1 and implies a tendency toward tilting or rotation of distorted MnO_6 octahedral framework of $AMnO_3$ (A = La, Sr, Ca, Bi). With increasing In concentration, (t) decreases (from 0.968 to 0.947) due to the increase in the average ionic radius of the B-site cation, which compresses the Mn–O–Mn bond angle and increases the Mn–O bond length[29] (Table 1).

3.2. Magnetic properties

Fig. 2 shows the temperature dependence of magnetization with field-cooled (FC) and zero field-cooled (ZFC) under a magnetic applied field of 0.05 T from $x = 0$ to $x = 0.3$.

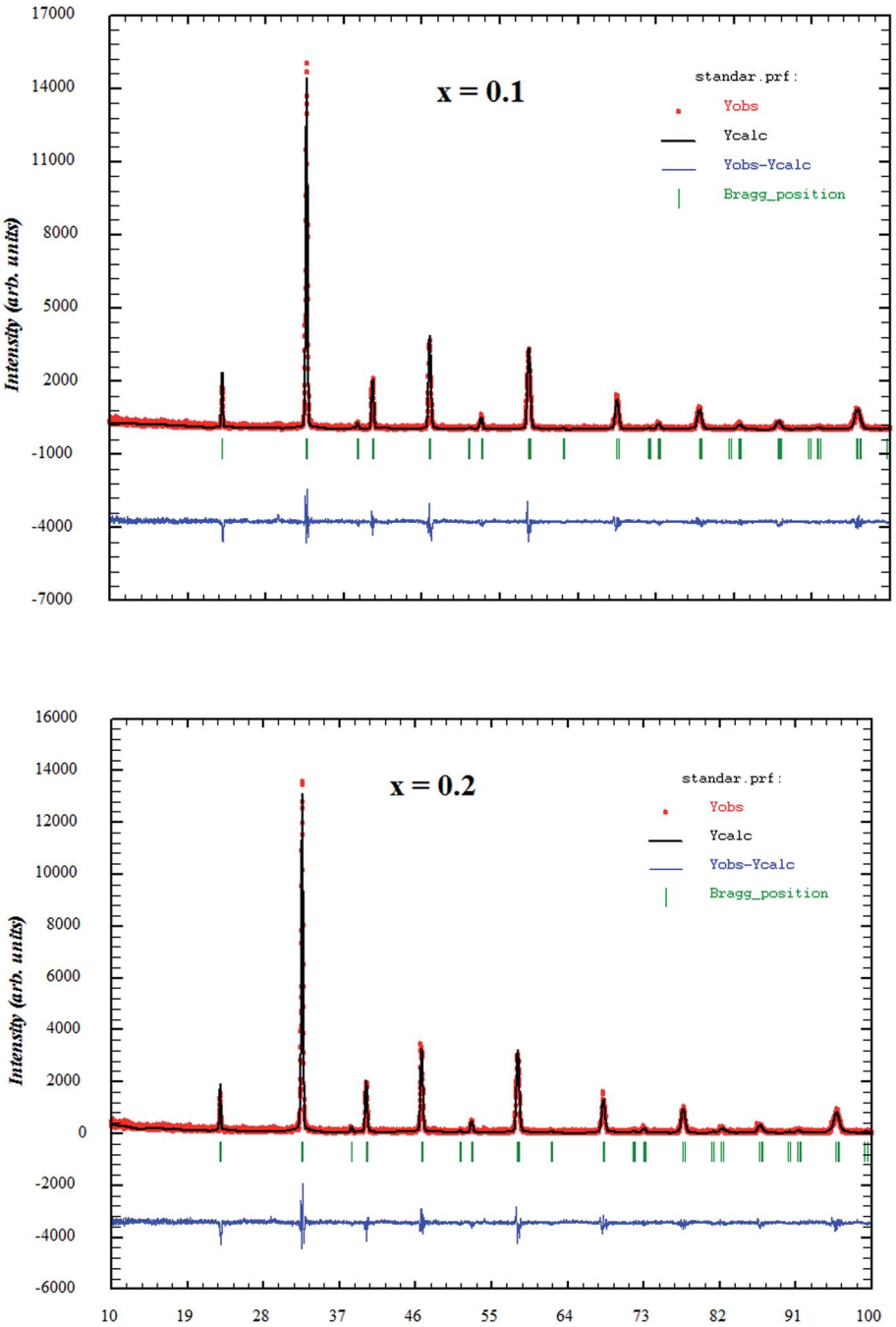

Fig. 1 Powder XRD patterns and Rietveld refinement result for $x = 0.1$ and $x = 0.2$.

All these samples exhibit a paramagnetic to ferromagnetic transition at the Curie temperature T_C. This temperature has been determined by differentiating the M–T curves and is defined as the inflection point of the function dM/dT. With increases of In doping, the Curie temperature T_C decreases from 330 K for $x = 0$ to 268 K for $x = 0.3$. This temperature reveals the long-range ferromagnetic ordering, indicating strong ferromagnetic exchange coupling between Mn and In sublattice.[30] In the low temperature region, FC and ZFC curves diverge significantly in all samples at the so-called irreversibility temperature (T*). This temperature is defined as the temperature below which M_{ZFC} departs from M_{FC} and large bifurcation starts to occur. We observe here that T* shifts to a lower temperature with an increase in In substitution and it is found to be 294 K, 266 K, 255 K, 245 K and 236 K for $x = 0$, $x = 0.1$, $x = 0.15$, $x = 0.2$ and $x = 0.3$, respectively. This splitting has been attributed to the magnetic frustration arising from a coexistence of insulating antiferromagnetic and metallic ferromagnetic phases, or from the competition between antiferromagnetic and ferromagnetic interactions. Moreover, the irreversibility for these samples demonstrates the signature of strong anisotropy field[31] generated from ferromagnetic (FM) clusters in the system. The

Table 1 Structural parameters determined from XRD data at room temperature for $La_{0.7}Bi_{0.05}Sr_{0.15}Ca_{0.1}Mn_{1-x}In_xO_3$ samples

	$x = 0$	$x = 0.1$	$x = 0.15$	$x = 0.2$	$x = 0.3$
Space group			$R\bar{3}c$		
Cell parameters					
a (Å)	5.6318 (2)	5.6434 (1)	5.6536 (4)	5.6576 (2)	5.6621 (1)
c (Å)	13.7733 (5)	13.7866 (2)	13.7954 (3)	13.8239 (2)	13.8704 (1)
V (Å^3)	378.33 (3)	380.25 (4)	381.87 (1)	383.20 (2)	385.10 (1)
Atoms					
La/Sr/Ca/Bi					
X	0	0	0	0	0
Y	0	0	0	0	0
Z	0.25	0.25	0.25	0.25	0.25
B_{iso} (La/Sr/Ca/Bi) (Å^2)	0.439 (3)	0.452 (5)	0.351 (5)	0.541 (2)	0.245 (2)
Mn/In					
X	0	0	0	0	0
Y	0	0	0	0	0
Z	0	0	0	0	0
B_{iso} (Mn/In) (Å^2)	0.379 (4)	0.384 (3)	0.248 (5)	0.423 (1)	0.265 (2)
O					
X	0.442 (2)	0.453 (1)	0.459 (3)	0.462 (1)	0.470 (6)
Y	0	0	0	0	0
Z	0.25	0.25	0.25	0.25	0.25
B_{iso} (O) (Å^2)	1.485 (5)	1.340 (3)	1.725 (5)	1.254 (2)	1.574 (4)
t	0.968	0.961	0.958	0.954	0.947
Bond lengths and bond angles					
d_{Mn-O} (Å)	1.955 (7)	1.967 (9)	1.971 (9)	1.973 (4)	1.984 (7)
$\theta_{Mn-O-Mn}$ (°)	173.20 (3)	166.08 (7)	165.14 (6)	164.49 (5)	161.45 (2)
Discrepancy factors					
R_P (%)	2.2	2.3	2.4	2.4	2.3
R_{WP} (%)	2.9	3.3	3.2	3.2	3.1
χ^2	1.26	1.63	1.37	1.55	1.44

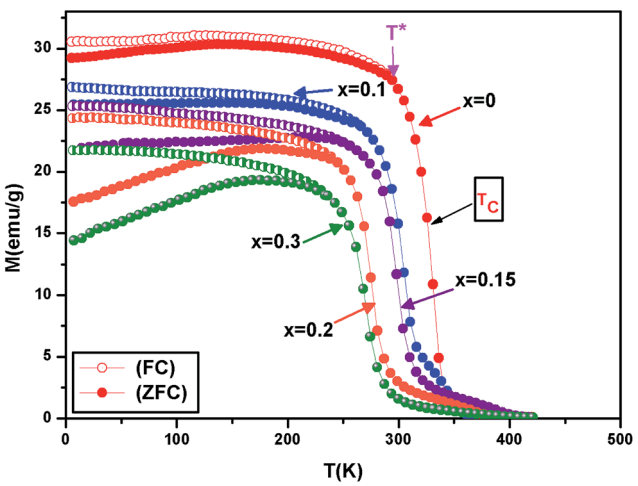

Fig. 2 Temperature dependence of magnetization under ZFC and FC curves at a field of 0.05 T for $La_{0.7}Bi_{0.05}Sr_{0.15}Ca_{0.1}Mn_{1-x}In_xO_3$.

magnetic moment gradually diminishes and prominent bifurcation between ZFC and FC curves become more and more obvious with increasing In concentration.[32] This phenomenon is observed in many magnetic materials.[33–36]

Furthermore, it is interesting to see which theoretical expression describes the temperature dependence of magnetization. According to Bloch's $T^{3/2}$ law, at a low temperature, the zero field magnetization $M(T,\mu_0H)$ should have a temperature dependence.[37]

$$M(T,\mu_0H)/M(0,\mu_0H) = 1 - BT^{3/2} \quad (2)$$

where $M(0,\mu_0H)$ and $M(T,\mu_0H)$ are the spontaneous magnetizations at $T = 0$ K and at finite temperature, respectively. The prefactor B is a constant characteristic of the spin waves at low temperature, which can be defined as:[38]

$$B = 2.612\left(\frac{g\mu_B}{M(0)}\right) \times \left(\frac{k_B}{4\pi D}\right)^{3/2} \quad (3)$$

where $g = 2$ is the gyromagnetic ratio for electron, k_B is the Boltzmann constant and μ_B is the Bohr magneton. Here D is the spin wave stiffness constant, which is defined by spin wave dispersion relation[39]

$$E(q) = \Delta + Dq^2 \quad (4)$$

here, $E(q)$ is the spin-wave energy, Δ is the gap energy arising from a magnetic anisotropy or an applied magnetic field μ_0H

and q is the momentum wave vector. It should be noted that for an FM of Heisenberg, $M(T)$ follows the law of Bloch $T^{3/2}$ generally in zero magnetic field. Under an external magnetic field, the variation of the magnetization with the applied field is more complex, as is observed in the dispersion spectra of spin waves which show the presence of a gap proportional to the applied magnetic field or anisotropy. However, Smolyaninova *et al.*[40] showed that the effect of the applied magnetic field is very low on the magnetization at low temperature. So we assume that $\Delta = 0$. In the inset (a) of Fig. 3, we show the curve $\ln(1 - (M(T,\mu_0H)/M(0,\mu_0H)))$ *versus* $\ln(T)$ of $x = 0.1$ for example, which is used to show that our samples obey Block's $T^{3/2}$ law. We have found that the slopes of all samples are closer to 1.4 (Table 2). It is predicted that the slope of the linear fit of these data must be close to 3/2. From eqn (2), the constant B represents the slope of the linear fit to the data of the $M(T,\mu_0H)/M(0,\mu_0H)$ *vs.* $T^{3/2}$ curve (shown in Fig. 3) and the values of D were determined. These curves show that our compounds approximately obey Bloch's $T^{3/2}$ law within range of low temperatures ($T \leq 100$ K). The values of B and D of all the samples are summarized in Table 2. This result shows that there is a spin wave excitation in our samples. The estimated D values are in good agreement with the previously reported result.[41–43]

We assume that the magnetic moment at temperature T and magnetic field μ_0H is given by

$$M(T,\mu_0H) = M_{Sp}(T) + \chi\mu_0H \quad (5)$$

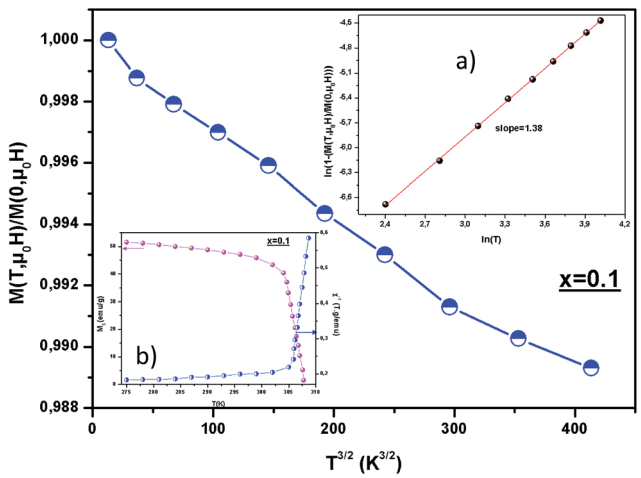

Fig. 3 Plots of $M(T,\mu_0H)/M(0,0)$ *vs.* $T^{3/2}$. The inset (a) shows the $\ln(1 - M(T,\mu_0H)/M(0,0))$ variation *vs.* $\ln(T)$ for $x = 0.1$. The inset (b): spontaneous magnetization M_{Sp} and the inverse susceptibility as a function of temperature for $x = 0.1$.

Table 2 Parameters determined from Bloch's $T^{3/2}$ law: slope, prefactor B, and spin stiffness constant D

	$x = 0$	$x = 0.1$	$x = 0.15$	$x = 0.2$	$x = 0.3$
Slope	1.43	1.38	1.46	1.40	1.51
B (10^{-5} K$^{-2/3}$)	2.91	2.70	2.03	1.85	1.69
D (meV Å^2)	97.76	112.56	143.38	156.83	181.75

The spontaneous magnetic moment of the sample can be obtained by fitting the linear part of magnetization at high magnetic field. The evolution of the spontaneous magnetization M_{Sp} and the susceptibility as a function of temperature, deduced from $M(\mu_0H)$ measurements, can be shown in the inset (b) of Fig. 3 for $x = 0.1$ for example. The $M_{Sp}(T)$ curve drops rapidly near $T_C = 310$ K, $T_C = 298$ K, $T_C = 275$ K and $T_C = 268$ K for $x = 0$, $x = 0.15$, $x = 0.2$ and $x = 0.3$, respectively showing a well-defined Curie temperature.

3.3. Magnetocaloric effect

The scope of this paper concerns the study of magnetocaloric effect (MCE), which is an intrinsic property of magnetic materials. It is the heating or cooling of materials when subjected to magnetic field variation, which is maximized when the material is near its magnetic ordering temperature.

Fig. 4 shows the magnetic-field dependences of the magnetization measured at different temperatures around T_C for $x = 0$ and $x = 0.15$ compounds for example. The magnetization was found to increase with decreasing temperature, where thermal fluctuations of spins decrease with decreasing temperature.

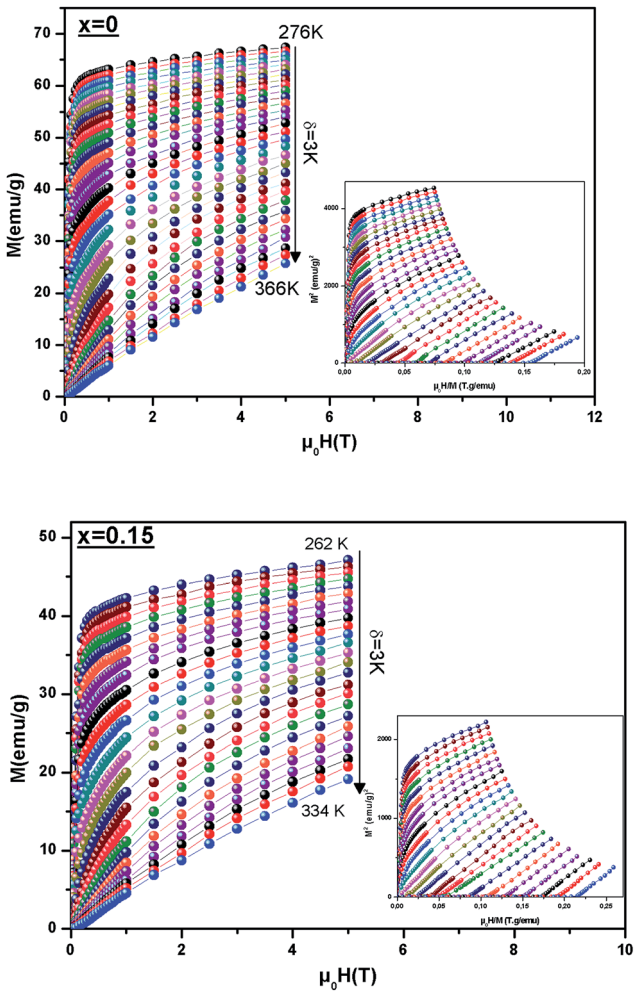

Fig. 4 Isothermal magnetization measured at different temperatures around T_C. The inset shows the Arrott plots for $x = 0$ and $x = 0.15$.

Therefore, in order to understand the nature of the magnetic phase transition, we can use the Banerjee criterion.[44] According to this law, the sign of slopes of the M^2 *vs.* μ_0H/M curves (Arrott plots) indicates the nature of the PM–FM transition; meaning that if a slope is negative, the transition is of first order (FOMT) while when it is positive, the transition is of second order (SOMT). The Arrott plots shown in inset of Fig. 4 clearly indicate a positive slope in the complete M^2 range, confirming the SOMT.

The MCE properties have been evaluated by calculating two factors:

(i) Magnetic entropy change (ΔS_M), which can be determined from the magnetization curves with the help of the Maxwell's relation given as:

$$\Delta S_M(T, \mu_0 H) = \int_0^{\mu_0 H} \left(\frac{\partial M(T, \mu_0 H)}{\partial T}\right) d(\mu_0 H) \quad (6)$$

(ii) and Relative Cooling Power (RCP), which is the most meaningful parameter that provides a measure of the amount of heat transfer between hot and cold sinks during one ideal refrigeration cycle. It is defined as:

$$RCP = -\Delta S_M^{max} \times \delta T_{FWHM} \quad (7)$$

where ΔS_M^{max} is the maximum entropy and δT_{FWHM} is a full width at half maximum and is defined as: $\delta T_{FWHM} = T_2 - T_1$; where T_1 and T_2 are the cold and hot temperatures.

In Fig. 5, we represent the temperature dependence of (ΔS_M) curve at different magnetic fields ranging from 1 to 5 T of $x = 0$ for example.

It is clear from this figure that the sign of the (ΔS_M) is negative, which means that heat is liberated when ($\mu_0 H$) is changed adiabatically. The value of (ΔS_M) grows up to a maximum value (ΔS_M^{max}) where the temperature approaches T_C and then decreases with increasing temperature. The obtained value of $x = 0$ for 5 T is about 62% of that presented by gadolinium metal (Gd). Gd, the reference for magnetocaloric materials, exhibits an isothermal entropy change of 5 J kg^{-1} K^{-1} and 9.8 J kg^{-1} K^{-1} for field changes of 2 T and 5 T, respectively.[45]

The evolution of (ΔS_M^{max}) with In^{3+} concentration is shown more clearly in the inset (a) of Fig. 5 We observed that (ΔS_M^{max}) drops with increasing substitution x, and exhibits values equal to 6.14 to 3.06 J kg^{-1} K^{-1} for $x = 0$ to 0.3 for 5 T.

An $\mu_0 H$ increase enhances (ΔS_M^{max}) and shifts the (ΔS_M^{max}) point gradually towards higher temperatures, which is indicative of a much larger entropy change being expected at higher magnetic fields (the inset (b) of Fig. 5).

The obtained RCP values of all samples are reported in Table 3, from which it can be clearly deduced that the substitution x decreases the value of the (RCP) factor from 281 J kg^{-1} for $x =$ 0 to 114 J kg^{-1} for $x = 0.3$ at 5 T. These values are comparable with those reported in literature.[45–49] From the inset (b) of Fig. 5, we observe that the RCP values exhibit a nearly linear dependence on the applied magnetic field.

3.4. Correlation between electrical and magnetic properties

It is well known that a strong correlation between the magnetic and electrical properties has been observed earlier.[50,51] In manganites, the CMR and MCE are usually observed around ferromagnetic–paramagnetic (FM)–(PM) transition temperature and we have tried to find a relationship between the change in magnetic entropy and resistivity for all samples. Using resistivity data, we can evaluate the magnetic entropy change by the relation as follows:[52]

$$\Delta S_M(T, \mu_0 H) = -\alpha \int_0^{\mu_0 H} \left(\frac{\partial Ln\rho}{\partial T}\right)_{\mu_0 H} d\mu_0 H \quad (8)$$

where α is the parameter, which determines the magnetic properties of sample. Such a relation between the magnetic and electrical properties were performed to estimate α directly[52]

$$\rho = \rho_0 \exp(-M/\alpha) \quad (9)$$

After that, O'Donnell *et al.*[50] studied this type of correlation and it was found that the exact relation should be:

$$\rho = \rho_0 \exp(-M^2/\alpha) \quad (10)$$

While Chen *et al.*[53] indicated that the resistivity is related to magnetization by the relation:

$$\rho = \rho_0 \exp(-M^2/\alpha T) \quad (11)$$

In Fig. 6, we can observe the variation of M, M^2 and M^2/T *versus* ln(resistivity) around T_C for sample $x = 0.15$ under a magnetic field of 2 and 5 T for example.

On the one hand, Fig. 6 shows that the resistivity strongly depends on M which indicates that the relation (9) is very suitable to describe the relationship between electrical and

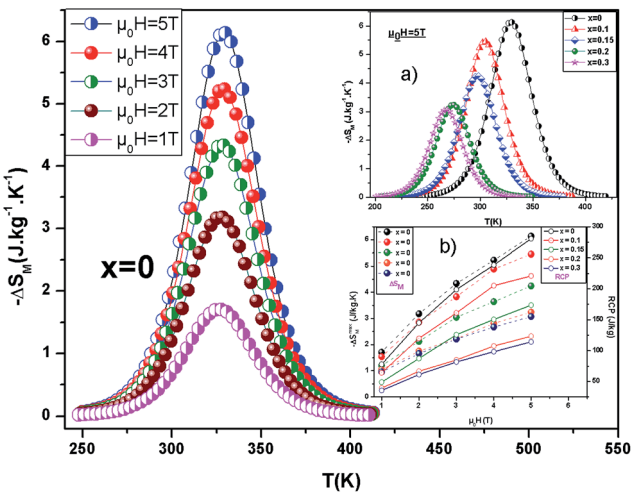

Fig. 5 Temperature dependence of the magnetic entropy change ($-\Delta S_M$) in various magnetic field of the compound $La_{0.7}Bi_{0.05}Sr_{0.15}Ca_{0.1}MnO_3$. The inset (a): magnetic entropy change as a function of temperature corresponding to an applied field 5 T for $La_{0.7}Bi_{0.05}Sr_{0.15}Ca_{0.1}Mn_{1-x}In_xO_3$ samples. The inset (b): maximum magnetic entropy change and RCP values as a function of $\mu_0 H$ for all samples.

Table 3 Comparison of the (MCE) properties between our samples and the others samples studied in the literature

Material	T_C (K)	$\mu_0 H$ (T)	ΔS_M^{max} (J kg^{-1} K^{-1})	RCP (J kg^{-1})	Ref.
$La_{0.7}Bi_{0.05}Sr_{0.15}Ca_{0.1}MnO_3$	330	5	6.14	281	This work
$La_{0.7}Bi_{0.05}Sr_{0.15}Ca_{0.1}Mn_{0.9}In_{0.1}O_3$	305	5	5.46	221	This work
$La_{0.7}Bi_{0.05}Sr_{0.15}Ca_{0.1}Mn_{0.85}In_{0.15}O_3$	298	5	4.26	173	This work
$La_{0.7}Bi_{0.05}Sr_{0.15}Ca_{0.1}Mn_{0.8}In_{0.2}O_3$	275	5	3.24	123	This work
$La_{0.7}Bi_{0.05}Sr_{0.15}Ca_{0.1}Mn_{0.7}In_{0.3}O_3$	268	5	3.06	114	This work
Gd	293	5	9.5	410	45
$Gd_5(Si_2Ge_2)$	275	5	18.5	535	46
$La_{0.75}Sr_{0.1}Ca_{0.15}MnO_3$	310	5	5.8	195	47
$La_{0.7}Sr_{0.25}Na_{0.05}MnO_3$	363	5	4.34	298	48
$La_{0.8}Ba_{0.1}Ca_{0.1}Mn_{0.85}Co_{0.15}O_3$	212	5	2.27	123	49

magnetic properties for all samples. On the other hand, we have found that the slope of the fitting data remains practically the same α (= 22.56 emu g^{-1}) even in different magnetic applied field for $x = 0.15$. Similar behavior was observed in all our samples.

Once the value of α was determined, we calculated magnetic entropy change around FM–PM transition for all samples, using the resistivity measurements as a function of magnetic applied field at several temperatures (Fig. 6).

Fig. 7 represents the variation of entropy change found from electrical and magnetic data as a function of temperatures at 5 T for sample $x = 0.15$. We can notice that the estimated values determined from ρ are found to agree with the experimental ones.

3.5. Prediction of electrical resistivity

The resistivity of manganite is determined by several parameters such as temperature, composition, the applied magnetic field, and so on. The effects of both applied magnetic field and temperature on the resistivity of our sample ($x = 0$) are shown in Fig. 8. All the samples display a clear metal–semiconducting (M–Sc) transition at a temperature T_{M-Sc}, which is obtained from the inflection point of $d\rho/dT$ plots. The tactful way to understand these properties of the samples based on the mathematical relationship between the resistivity and the temperature or the magnetic field is to fit these curves. This prediction of the electrical resistivity was reported by changshi.[54] According to their suggestion, the Gauss function which is a typical numerical method with a nonlinear curve fitting for the quantitative analysis, offers such an opportunity. The Gauss function is given by

$$\rho(T) = \rho(T_u) + \frac{A}{w\sqrt{\pi/2}} \exp\left(-2(T - T_d)^2 \Big/ w^2\right) \quad (12)$$

where $\rho(T_u)$, A, T_d, and w are constants obtained from the fitting process.

If the Gauss function is available for predicting electrical resistivity (ρ) in all the temperature ranges for LBSCMO, the minimum value of ρ is given by $\rho(T|_{T\to\infty})$. Therefore, the physical signification of parameter $\rho(T_u)$ is the electrical resistivity of manganite materials at high temperatures. The maximum value for ρ is given in the following equation

$$\rho_{max} = \rho|_{T\to\infty} + \frac{A}{w\sqrt{\pi/2}} \quad (13)$$

So, eqn (12) will be rewrite as:

$$\rho(T) = \rho_{min} + \frac{A}{w\sqrt{\pi/2}} \exp\left(-2(T - T_d)^2 \Big/ w^2\right) \quad (14)$$

Then, the experimental data, have been simulated using eqn (14) which, are shown in the inset of Fig. 8 for $x = 0$ for example and the results are presented in table in ESI.†

To verify the accuracy of this simulation, the correlation coefficient (R^2) of the simulated with experimental data is given in table in ESI.† The correlation coefficient, which was close to 1, showed a satisfactory agreement between experimental and the modeled data. The comparison between the peaks of the experimental data and the best-fitted value of T_d, calculated from Gauss function, demonstrated that parameter T_d corresponds to the metal–semiconducting transition temperature, T_{M-Sc}.

Therefore, T_{M-Sc} can be confirmed more precisely by the appropriate Gauss function simulation for other magnetic fields.

Fig. 9 shows the dependency of ρ_{max} on the applied magnetic field for $x = 0$ for example. The best fitted results demonstrate that the logistic equation could properly give a quantitative relationship between ρ_{max} and ($\mu_0 H$) using the non-linear curve fitting, and the logistic relation is defined as

$$\rho_{max}(\mu_0 H) = A + \frac{A - B}{1 + \left(\frac{\mu_0 H}{C}\right)^P} \quad (15)$$

where A, B, C and P are constant and will be determined from the fitting of the experimental data (Table 4).

This logistic function successfully describes the experimental behavior of the maximum electrical resistivity of all samples. According to this model, it can be observed that the maximum resistivity decreases with an increasing magnetic field. This phenomenon implies that the density of charge carriers increases with the increasing of the applied magnetic field. Therefore, it is important to use this model for predicting

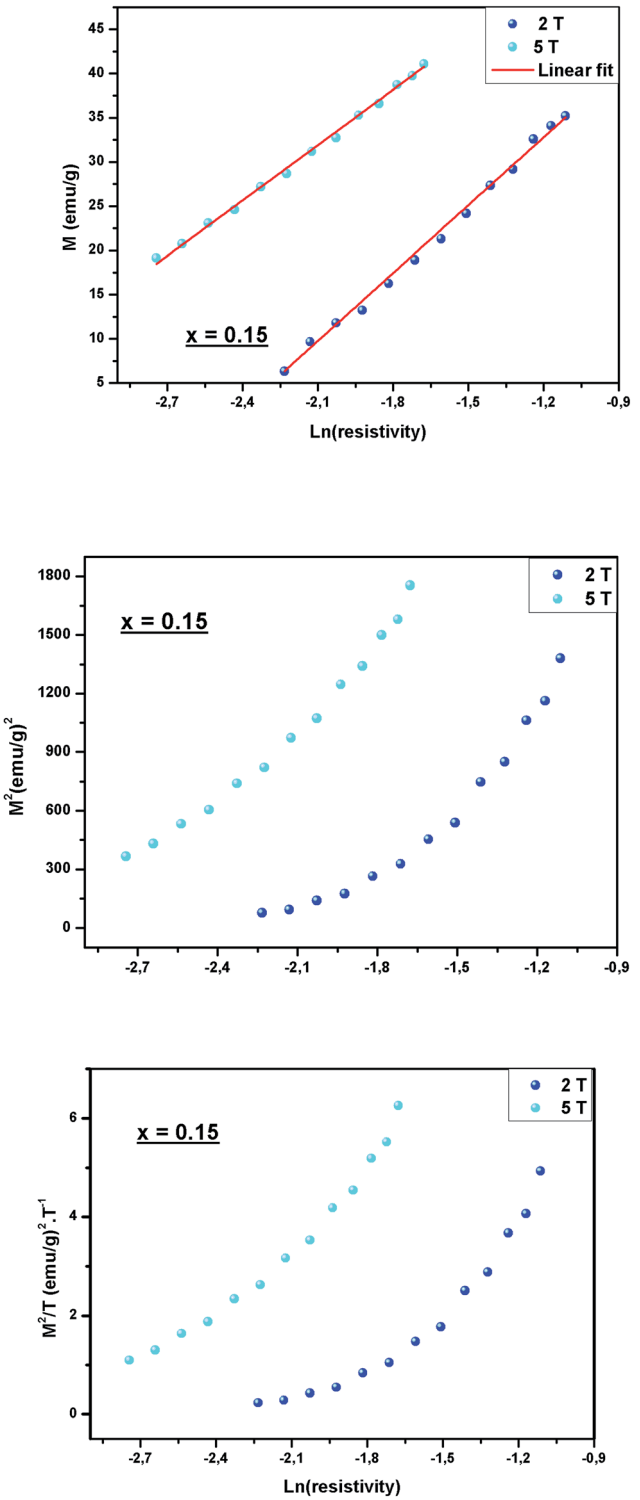

Fig. 6 M, M^2 and M^2/T *versus* ln(resistivity) for $x = 0.15$ compound, under the field of 2 and 5.

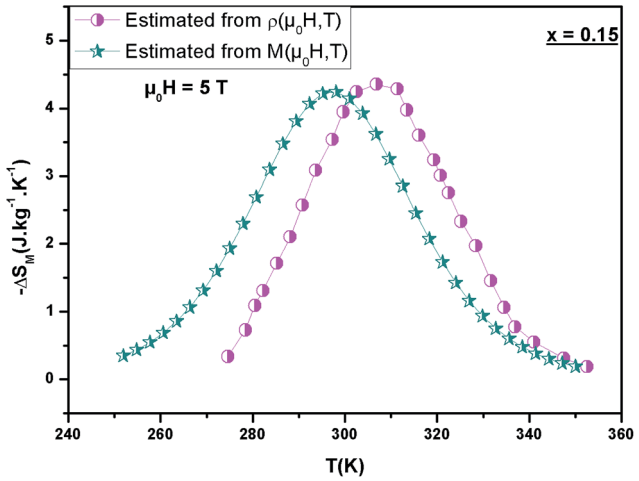

Fig. 7 Temperature dependence of the $(-\Delta S_M)$ measured from $M(\mu_0 H,T)$ and determined from $\rho(\mu_0 H,T)$ under $\mu_0 H = 5$ T for $La_{0.7}Bi_{0.05}Sr_{0.15}Ca_{0.1}Mn_{0.85}In_{0.15}O_3$.

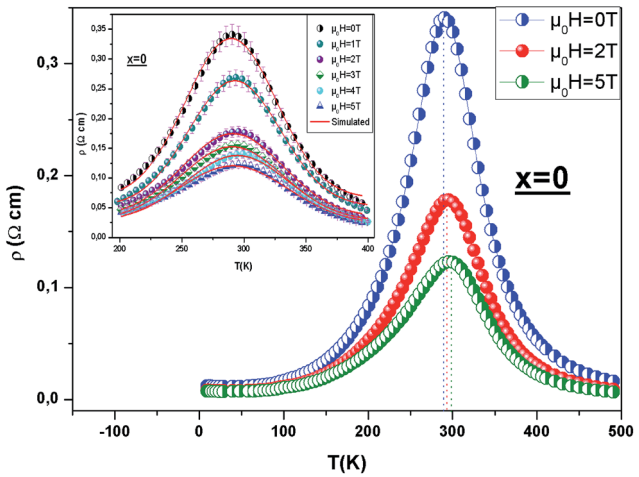

Fig. 8 Resistivity *vs.* temperature curves of $x = 0$ under different applied magnetic fields rising from 0 to 5 T. The inset: experimental (symbol) and estimated (line) electrical resistivity as a function of temperature of $x = 0$ under different applied magnetic field.

the maximum electrical resistivity, before applying the magnetic field.

From Fig. 8, it has been seen that when $\mu_0 H$ increases, T_{M-Sc} of all samples shifts toward higher temperatures, which can confirm that T_{M-Sc} is related to the applied magnetic field.

The T_{M-Sc} as a function of magnetic field is shown in the inset of Fig. 9 for $x = 0$ for example.

From this figure, we can see, that there is a simple linear relationship between these two parameters. The equation that describes this relationship is written as:

$$T_{M-Sc}(\mu_0 H) = S \times (\mu_0 H) + I \quad (16)$$

The obtained constants are illustrated in Table 4.

Impressively, it seems that the theoretical results for T_{M-Sc} derived by eqn (16) were proportional to the experimental results. Therefore, it can be concluded that $\mu_0 H$ is correlative with T_{M-Sc}. Also, it is feasible that eqn (16) is used to investigate the potential shifts of T_{M-Sc} by applying magnetic field. The shifts of the T_{M-Sc} to the high-temperature range with the application of the magnetic field may occur because of the

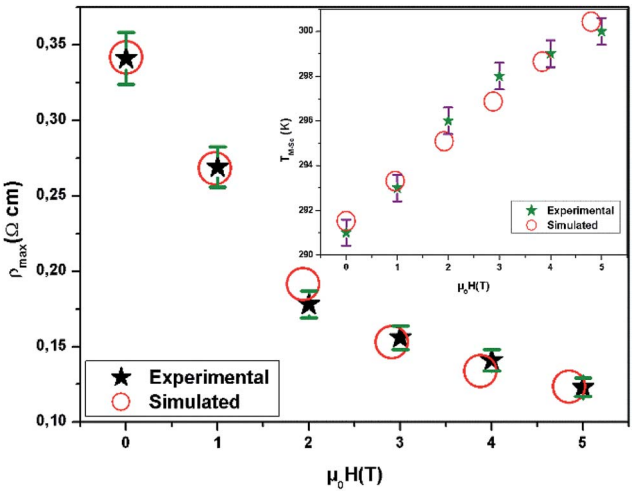

Fig. 9 Experimental and simulated ρ_{max} as a function of magnetic field. The inset: T_{M-Sc} *vs.* $\mu_0 H$ for $La_{0.7}Bi_{0.05}Sr_{0.15}Ca_{0.1}MnO_3$ compound.

Table 4 The obtained constants determined fitting the experimental data using eqn (15) and (16)

	$x = 0$	$x = 0.1$	$x = 0.15$	$x = 0.2$	$x = 0.3$
A	0.101	0.161	0.121	0.202	0.196
B	−0.141	−0.212	−0.495	−0.698	−1.237
C	1.489	1.230	1.578	1.112	1.134
P	1.912	2.241	1.594	1.878	1.845
S	1.857	2.086	1.771	1.771	3.210
I	291.524	278.285	263.904	257.904	247.333

reduction in the charge carriers delocalization caused by applied magnetic field, which could result in reducing the resistivity. This field also uniformly caused a local spin ordering and due to this ordering, the ferromagnetic metallic state could overcome the semiconducting regime. Consequently, the conduction electrons (e_g^1) are completely polarized within the magnetic domains and could easily be transferred between the pairs of Mn^{3+} ($t_{2g}^3 e_g^1$: $S = 2$) and Mn^{4+} ($t_{2g}^3 e_g^0$: $S = 3/2$) *via* oxygen. So, T_{M-Sc} shift to higher temperatures.

4. Conclusion

In conclusion, we have mainly studied the magnetic and magnetocaloric properties of $La_{0.7}Bi_{0.05}Sr_{0.15}Ca_{0.1}Mn_{1-x}In_xO_3$ with x = 0–0.3. The magnetization *vs.* temperature curve is explained by the presence of the spin glass state in all samples in low temperature arising in the ZFC process and showing a sharp transition from paramagnetic to ferromagnetic phase at T_C. According to the Arrott plots, we have found that all our samples have a second order magnetic phase transition. The (MCE) can be determined by direct and indirect methods. First, based on the magnetic measurement at applied field of $\mu_0 H = 5$ T, $La_{0.7}Bi_{0.05}Sr_{0.15}Ca_{0.1}Mn_{1-x}In_xO_3$ samples exhibit a maximum value of (ΔS_M) which decreases from 6.14 J kg^{-1} K^{-1} for $x = 0$ to 3.06 J kg^{-1} K^{-1} for $x = 0.3$ with increasing In content and thus the RCP values also decrease. The large MCE, found in these samples, suggests that its can be considered as a promising potential candidate for magnetic refrigeration application. Second, from the temperature dependence of resistivity, we have succeeded to evaluate the (ΔS_M). On the other hand, the resistivity was fitted using the mathematical model (Gauss function). The perfect agreement between the theoretical and the experimental values of T_{M-Sc} and ρ_{max} is obtained.

References

1 R. N. Mahato, K. Sethupathi, V. Sankaranarayanan and R. Nirmala, *J. Appl. Phys.*, 2010, **107**, 09A943.
2 H. Choi, E. Y. Kim and C. M. Whang, *Electron. Mater. Lett.*, 2011, **7**, 231.
3 M. S. Anwar, S. Kumar, F. Ahmed, S. N. Heo, G. W. Kim and B. H. Koo, *J. Electroceram.*, 2013, **30**, 46.
4 R. P. Pawar, R. N. Jadhav and V. Puri, *Electron. Mater. Lett.*, 2012, **8**, 321.
5 M. S. Anwar, S. Kumar, F. Ahmed, N. Arshi and B. H. Koo, *Mater. Res. Bull.*, 2012, **47**, 2977.
6 H. E. Kim, K. H. Choi, M. W. Park and J. S. Lee, *Electron. Mater. Lett.*, 2011, **7**, 319.
7 C. Zener, *Phys. Rev.*, 1951, **82**, 403.
8 S. Jin, T. H. Tiefel, M. McCormack, R. A. Fastnacht, R. Ramesh and C. H. Chen, *Science*, 1994, **264**, 413.
9 R. V. Holmolt, J. Wocker, B. Holzapfel, L. Schultz and K. Samwer, *Phys. Rev. Lett.*, 1993, **71**, 2331.
10 A. P. Ramirez, *J. Phys.: Condens. Matter*, 1997, **9**, 8171.
11 Y. Tokura, *Rep. Prog. Phys.*, 2006, **69**, 797.
12 A. Dinesen and J. Tejada, *J. Phys.: Condens. Matter*, 2005, **17**, 6257–6269.
13 D. N. H. Nam, N. V. Dai, L. V. Hong, N. X. Phuc, S. C. Yu, M. Tachibana and E. Takayama-Muromachi, *J. Appl. Phys.*, 2008, **103**, 043905.
14 N. Chau, P. Q. Niem, H. N. Nhat, N. H. Luong and N. D. Tho, *Phys. B*, 2003, **327**, 214.
15 M. Phan, S. Tian, D. Hoang, S. Yu, C. Nguyen and A. Ulyanov, *J. Magn. Magn. Mater.*, 2003, **258**, 309–311.
16 M.-H. Phan and S.-C. Yu, *J. Magn. Magn. Mater.*, 2007, **308**, 325–340.
17 M.-H. Phan, N. D. Tho, N. Chau, S.-C. yu and M. Kurisu, *J. Appl. Phys.*, 2005, **97**, 103901.
18 A. P. Ramirez, *J. Phys.: Condens. Matter*, 1997, **9**, 8171.
19 D. Louca, T. Egami, E. L. Brosha, H. Röder and A. R. Bishop, *Phys. Rev. B: Condens. Matter Mater. Phys.*, 1997, **56**, R8475(R).
20 C. M. Xiong, J. R. Sun, Y. F. Chen, B. G. Shen, J. Du and Y. X. Li, *IEEE Trans. Magn.*, 2005, **41**, 122–124.
21 N. Zaidi, S. Mnefgui, J. Dhahri and E. K. Hlil, *Ceram. Int.*, 2016, **42**, 17687–17692.
22 A. Zaidi, T. Alharbi, J. Dhahri, S. Alzobaidi, M. A. Zaidi and E. K. Hlil, *Appl. Phys. A*, 2017, **123**, 94.
23 V. Punith Kumar, R. L. Hadimani, D. Paladhi, T. K. Nath, D. C. Jiles and V. Dayal, *Mater. Sci. Eng., B*, 2016, **209**, 75–86.
24 M. Pechini, *US Pat.* no. 3330697, 1967.
25 H. M. Rietveld, *J. Appl. Crystallogr.*, 1969, **2**, 65.

26 T. Roisnel and J. Rodriguez-Carvajal, Computer Program FULLPROF, LLB-LCSIM, May, 2003.
27 R. D. Shannon, *Acta Crystallogr., Sect. A: Cryst. Phys., Diffr., Theor. Gen. Crystallogr.*, 1976, **32**, 751–767.
28 V. M. Goldschmidt, *Geochemistry*, Oxford University Press, Oxford, 1958, p. 730.
29 N. Moutis, I. Panagiotopoulos, M. Pissas and D. Niarchos, *Phys. Rev. B: Condens. Matter Mater. Phys.*, 1999, **59**, 1129.
30 V. Markovich, I. Fita, R. Puzniak, A. Wisniewski, K. Suzuki, J. W. Cochrane, Y. Yuzhelevskii, Y. M. Mukovskii and G. Gorodetsky, *Phys. Rev. B: Condens. Matter Mater. Phys.*, 2005, **71**, 224409.
31 J. Kuo and G. Sheng-Kai, *Chin. Phys. B*, 2009, **18**, 3035.
32 A. K. Pramanik and A. Banerjee, *Phys. Rev. B: Condens. Matter Mater. Phys.*, 2009, **79**, 214426.
33 J. Mira, J. Rivsa, F. Rivadulla, C. V. Vazquez and M. A. L. Quintela, *Phys. Rev. B: Condens. Matter Mater. Phys.*, 1999, **60**, 2998.
34 D. N. H. Nam, K. Jonason, P. Nordblad, N. V. Khiem and N. X. Phuc, *Phys. Rev. B: Condens. Matter Mater. Phys.*, 1999, **59**, 4189.
35 D. N. H. Nam, R. Mathieu, P. Nordblad, N. V. Khiem and N. X. Phuc, *Phys. Rev. B: Condens. Matter Mater. Phys.*, 2000, **62**, 1027.
36 M. Itoh, I. Natori, S. Kubota and K. Motoya, *J. Phys. Soc. Jpn.*, 1994, **63**, 1486.
37 B. Padmanabhan, S. Elizabeth, H. L. Bhat, S. RoBler, K. Dorr and K. H. Muller, *J. Magn. Magn. Mater.*, 2006, **307**, 288–294.
38 F. E. Luborsky, *Ferromagnetic Materials*, Elsevier, Amsterdam, 1979.
39 C. Kittel, *Quantum Theory Solids*, Wiley, New York, 1993.
40 V. N. Smolyaninova, J. J. Hamilton, R. L. Greene, Y. M. Mukovskii, S. G. Karabashev and A. M. Balbashov, *Phys. Rev. B: Condens. Matter Mater. Phys.*, 1997, **55**, 5640.
41 P. Dai, J. A. Fernandez-Baca, E. W. Plummer, Y. Tomioka and Y. Tokura, *Phys. Rev. B: Condens. Matter Mater. Phys.*, 2001, **64**, 224429–224434.
42 B. Padmanabhan, S. Elizabeth, H. L. Bhat, S. Rossler, K. Dorr and K. H. Muller, *J. Magn. Magn. Mater.*, 2006, **307**, 288–294.
43 A. Tozri, E. Dhahri and E. K. Hlil, *J. Magn. Magn. Mater.*, 2010, **322**, 2516–2524.
44 B. K. Banerjee, *et al.*, *Phys. Lett.*, 1964, **12**, 16–17.
45 V. K. Pecharsky and K. A. Gshneidner Jr, *J. Magn. Magn. Mater.*, 1997, **167**, L179.
46 K. A. Gschneidner Jr, V. K. Pecharsky and A. O. Tsokol, *Rep. Prog. Phys.*, 2005, **68**, 1479.
47 A. Dhahri, M. Jemmali, E. Dhahri and M. A. Valente, *J. Alloys Compd.*, 2015, **638**, 221–227.
48 S. E. Kossi, S. Ghodhbane, S. Mnefgui, J. Dhahri and E. K. Hlil, *J. Magn. Magn. Mater.*, 2015, **395**, 134–142.
49 M. A. Gdaiem, A. Dhahri, J. Dhahri and E. K. Hlil, *Mater. Res. Bull.*, 2017, **88**, 91–97.
50 J. O'Donnell, M. Onellion, M. S. Rzchowski, J. N. Eckstein and I. Bozovic, *Phys. Rev. B: Condens. Matter Mater. Phys.*, 1996, **54**, 6841.
51 B. Chen, C. Uher, D. T. Orelli, J. V. Mantese, A. M. Mance and A. L. Micheli, *Phys. Rev. B: Condens. Matter Mater. Phys.*, 1995, **53**, 5094.
52 C. M. Xiong, J. R. Sun, Y. F. Chen, B. G. Shen, J. Du and Y. X. Li, *IEEE Trans. Magn.*, 2005, **41**, 122.
53 B. Chen, C. Uher, D. T. Orelli, J. V. Mantese, A. M. Mance and A. L. Micheli, *Phys. Rev. B: Condens. Matter Mater. Phys.*, 1995, **53**, 5094.
54 L. Changshi, *J. Chem. Eng. Data*, 2011, **56**, 2.